García Martínez, A.; Monsalve-Serrano, J.; Lago-Sari, R.; Martínez-Boggio, SD. (2022). Influence of environmental conditions in the battery thermal runaway process of different chemistries: Thermodynamic and optical assessment. International Journal of Heat and Mass Transfer. 184:1-14. https://doi.org/10.1016/j.ijheatmasstransfer.2021.122381

Influence of environmental conditions in the battery Thermal Runaway Process of different chemistries: Thermodynamic and Optical assessment

Antonio García*, Javier Monsalve-Serrano, Rafael Lago Sari, Santiago Martinez-Boggio

CMT - Motores Térmicos, Universitat Politècnica de València, Camino de Vera s/n, 46022 Valencia, Spain

International Journal of Heat and Mass Transfer
Volume 184, March 2022, 122381
https://doi.org/10.1016/j.ijheatmasstransfer.2021.122381

Corresponding author (*):
Dr. Antonio García (angarma8@mot.upv.es)
Phone: +34 963876574

Abstract

Thermal runaway is one of the main concerns of battery electric vehicles due to the hazard level that represents for the user and the surroundings. Several works studied different type of abuse in lithium-ion cells and packs, but the understanding is still insufficient in terms of the combustion process. In this study, three different lithium-ion cell chemistries (LCO, NMC and LFP) are studied in two environmental conditions with different oxygen content (0% and 21%) in a continuous flow vessel to understand if the use of inert atmosphere may be a pathway to avoid thermal runaway. In addition, detailed optical research is conducted together with temperature sensing to understand the venting through the vent cap before the thermal runaway. The combustion is recorded with a high-speed camera (6,000 fps) while the venting is visualized through a Schlieren technique with another high-speed camera (12,000 fps). The thermodynamic results show that the venting process can be detected by a cell surface temperature decrease of around 5ºC, while the thermal runaway is seen as a battery self-heating (cell temperature higher than the ambient) and a suddenly increase of temperature until 700ºC in the surface of the cell. The optical access to the combustion chamber allows to observe with detail the venting of liquid electrolyte among the gases generated by the thermal abuse. In addition, the combustion records show that with inert atmosphere the combustion it is not initiated, and the process is restricted to smoke ejection. By contrast, the case of air (21% O_2) resulted in combustion outside the battery cell with high increase of the air temperature. In terms of battery chemistry, the Lithium, Ferrum, Phosphate (LFP) shows the highest safety time and lowest chamber temperatures. LCO and Nickel Manganese Cobalt (NMC) had similar behavior in terms of safety time and temperature behavior, but Lithium Cobalt Oxygen (LCO) shows more variation with respect to the atmosphere (reactive and inert) than NMC.

Keywords

Battery Thermal Runaway; Electric Vehicles; Fire; Lithium-Ion Battery; Safety

1. Introduction

Alarming reports published in the last years have been reinforcing the need of reducing the carbon dioxide emissions produced by human activities [1][2][3]. Recently, the Intergovernmental Panel on Climate Change (IPCC) have provided light on the possible scenarios that may occur in case of that no measures are applied to control de CO_2 emissions, pointing that the average temperature in the earth could increase from 1.2^{o}C to 1.9^{o}C by 2040 [4]. Considering these studies, most of the countries are releasing new pledges to avoid such a catastrophic scenario [5]. Specifically in the transportation sector, which is responsible by 18% of the total CO_2 emissions emitted in the energy sector in Europe [6], mandates that prone the fast introduction of battery electric vehicles are being approved. As per, Europe has considered to ban the sales of new internal combustion engine vehicles by 2030 [7]. However, this ambitious plan still faces several contradictory arguments. First, electric vehicles still emit CO_2 in a life-cycle basis, being heavily dependent on the energy matrix that is used for charging the batteries [8]. Additionally, the infrastructure needed must be fully deployed, requiring incentives to install fast chargers in urban, highway and rural areas [9]. Nonetheless, one of the most concerning issues relies on the safety matters that are related to this propulsion system. Different reports and news have stressed the battery fire hazards that may occur during vehicle operation or charging [10]. This alarming issue, generally originated by a phenomenon called battery thermal runaway (BTR) has a devastating potential, threatening the passenger life [11]. In this sense, it is considered that the understanding of these phenomenon and how to mitigate it on a battery cell level is of utmost importance to guarantee the successful deployment of battery electric vehicles in the market [12][13].

In this sense, different investigations have been performed aiming at improving the understanding of the BTR from kinetic based analysis to complete module response [14][15][16]. On the kinetic side, Hatchard et al. [17] pioneered on proposing an Arrhenius based description for the different decomposition reactions that may lead to the thermal runaway occurrence. They identified that the SEI decomposition may releases organic compounds that reacts with the oxygen with the cathode in an exothermic way. As the temperature increases, the exponential dependence of the reaction rates with the temperature leads to an accelerating process. In case of having an excessive decomposition of the solid electrolyte interface, an internal short circuit may occur, opening new pathways of the decomposition from the cathode and anode reactions, which provides an abrupt energy release and possible fire occurrence. Different authors [18] [19] have followed the modelling approach proposed by Hatchard et al. [17], improving the number of reactions accounted for the thermal runaway description or enhancing the modelling for other battery chemistries.

The battery chemistries play a dominant role on the thermal stability of the battery cell and, consequently, on the battery thermal runaway occurrence [20][21]. Currently, the most used battery cathode chemistries in the automotive sector are Nickel Manganese Cobalt (NMC), Lithium, Ferrum, Phosphate (LFP) and Lithium Cobalt Oxygen

(LCO) [22]. While NMC cells present a high energy capacity they have a low thermal stability compared to LFP battery cells. Investigations performed on accelerated rate calorimeters have identified that both cell venting and the thermal runaway onset takes places at lower temperatures for the NMC 811 compared to a LFP cell [20][23]. Another factor that can influence the thermal runaway occurrence is the environment at which the cells are exposed. Chen et al. [24] has assessed the influence of different environment pressures aiming at simulating the utilization of 18650 LCO battery cells at high altitudes. They have observed that the thermal runaway is highly dependent on the ambient pressure. Low values of external pressure led to early thermal runaway occurrence and higher peak temperatures. Guo et al. [25] have also investigated the effect of the environment temperature on the thermal runaway occurrence, considering 18650 LCO batteries during the study. The results suggested that despite of achieving the temperature onset in small times, high environment temperature values did not change the thermal runaway onset, indicating that the chemistry of the battery plays a dominant role on defining the thermal runaway occurrence.

Despite the different evaluations, the effect of the atmosphere composition was still not addressed. It is believed that the use of inert atmosphere could offer a way to decrease the impact of the thermal runaway of a battery cell over the pack. Recently, Weng et al. [26] has identified that the reduction of the oxygen concentration reduces the thermal runaway propagation speed by 44%. Nonetheless, no extra evidence is found in the literature, at the best of the authors knowledge, where comparisons between inert and reactive environments are used during the cell evaluation. Additionally, most of the studies are restricted to provide only temperature and voltage measurements of the battery cell for a unique battery chemistry [27]. Although the importance of these parameters is clear, changes in the environment may change not only the battery related parameters but also the succession of phenomena that may occur with the vented gases in the environment at which the battery is exposed. For this type of analysis, more sophisticated assessment techniques rather than only temperature measurements should be used such as fast imagining. However, the application of this techniques is still restricted in the battery investigation field.

In this sense, this work aims at evaluating the effect of the environment composition on the thermal runaway evolution for different battery chemistries by means of both thermodynamic and optical measurement techniques. 18650 LCO, NMC and LFP battery cells with 100% of SOC were tested in a continuous flow vessel (CFV) test bed using a temperature ramp of 11^{o}C/min for all the cases. The continuous flow allows enhance the visualization of the battery venting and combustion. Inert and reactive environment were promoted inside of the vessel by using N_2 or synthetic air (O_2+N_2) as working gas, respectively. Schlieren and natural luminosity techniques were employed to identify the venting pattern of the ejected flow from the battery cell as well as its nature (liquid or solid) and to compare the evolution of the combustion process for each case. In spite of that in the literature can be found several works studying inert atmosphere and different cathode materials [28][29] as well as battery thermal management [30][31], the main novelty of this work is the study through detailed venting and thermal runaway images that can help to understand how the phenomena initiate and propagate outside the battery cell. Up to the knowledge of the authors, this work includes a unique thermal runaway description by high speed visualization and there are no works in the bibliography that have this information.

2. Experimental tools

This section intends to describe in detail the experimental facilities used during this investigation as well as the different optical techniques to assess the BTR phenomenon.

2.1. Lithium-Ion battery cell

For this study, three different cells were used to understand the effect of the battery chemistry and electrical characteristics in the thermal runaway process. Lithium Cobalt Oxide ($LiCoO_2$) also named as ICR or LCO, Lithium Manganese Nickel ($LiNiMnCoO_2$) also named as INR or NMC and Lithium Iron Phosphate ($LiFePO_4$) also named as IFR or LFP were taken for the study. Samsung 26J (LCO), Samsung 20R (NMC) and NX 9073 (LFP) commercial lithium-ion batteries are used. Among the cathode chemistry differences, the nominal capacity and electrical characteristics changes with a range from 2.6 to 1.8 Ah. The size is maintained, being all cylindrical cells 18650 (18 mm diameter and 65 mm height) with similar total weight (≈43.5 grams). In terms of safety, the battery cells have a vent cap to release the pressure when submitted to an abuse. In this case, the LCO Samsung 26J has 6 symmetric holes and the other two cells have 3 holes. For this study all cells are tested in maximum state of charge (SOC = 100%), charged by a constant current of 1C until reaching the maximum voltage and then charged at maximum voltage until the current goes to zero as suggested by the manufacturers. During the charging, the ambient temperature is maintained at 20°C and the battery under natural convection cooling ($h \approx 5$ W/m^{2}K). Detailed information about the battery cells can be found in Table 1.

Overall, LCO are the most common type of Lithium-Ion cell with a high energy content but low charge and discharge current. On the other hand, NMC has less capacity and available energy but can deliver higher current rates. Lastly, LFP is characterized by a low voltage operation and similar discharging rate than the LCO.

Table 1 – Main Lithium-Ion Samsung 26J battery cell properties.

Parameter	**ICR (Samsung 26J)**	**INR (Samsung 20R)**	**IFR (NX 7063)**
Cell Origin [-]	Purchase in free market		
Cell format [-]	18650		
Dimensions [mm]	18.3 x 65.0		
Cathode Chemistry [-]	LCO	NMC	LFP
Weight [g]	44.18 ± 0.19	43.21 ± 1.16	40.87 ± 0.02
Nominal Capacity [Ah]	2.6	2.0	1.8
Nominal Voltage [V]	3.6	3.6	3.2
Current Charge Continuous/Peak [A]	1.3/2.6	1.0/4.0	1.8/NA
Charging Time Normal/Rapid [min]	180/150	180/50	110/NA
Current Discharge Continuous/Peak [A]	5.2/NA	22/NA	5.4/10$_{@5s}$
Energy [Wh]	9.36	7.20	5.76
Energy density gravimetric [Wh/kg] / volumetric [Wh/L]	210/566	162/435	139/348

Vent Cap holes	6 holes	3 holes	3 holes
Voltage at 100% SOC [V]	4.02	4.15	3.65
Cut-off voltage [V]	2.75	2.50	2.50
State of Charge for testing in CFV [%]	100		

*Energy [Wh]= Nominal Capacity [Ah] x Nominal Voltage [V]

2.2. Continuous Flow Vessel

Each one of the battery cells described previously were exposed to controlled environments regarding temperature, pressure, and composition. This was attained by means of using a continuous flow vessel (CFV). This vessel is well documented and has been used in different fundamental evaluations for spray and combustion analysis at controlled conditions [32][33]. For this study, the CFV was adapted by building a new holder for the battery and supports for thermocouples to monitor the battery temperature. The holder enhances the air homogeneity while protects the direct impact of the hot air with the battery prior the mixing inside the vessel. This experimental apparatus was designed to support temperatures up to 1370^{o}C and an internal pressure of 150 bar, presenting approximately 40 L in volume. A scheme of the experimental set up is shown in Figure 1. Thermocouples type K were used to monitor the temperature increase at three different locations of the battery cell (bottom, center and top) and on the continuous flow vessel Environment. The thermocouples present a measurement range from -200 ^{o}C to 1260 ^{o}C and a total uncertainty of ±2.5^{o}C.

This device offers several benefits such as the ability of controlling the heating rate, mass flow rate and composition of the internal volume at which the battery is inserted. The mechanisms behind each actuation are illustrated in **¡Error! No se encuentra el origen de la referencia.**. Both temperature and pressure in the chamber are controlled by means of a closed loop actuation based on proportional integral derivative (PID) controllers. The feedback signals (temperature and pressure) to feed the PID are obtained inside of the vessel. In particular, the temperature is increased by external heaters and the pressure by regulating the compressor outlet pressure and the valve downstream the vessel. Therefore, for this CFV it is possible to achieve 1370^{o}C and a range of pressure between 2.6 bar to 150 bar. The minimum pressure cannot be decreased in the CFV due to the minimum amount of gas in the inlet to protect the resistance. As in this experiment is wanted to replicate real battery application, the minimum is set. The system contains different safety management devices that guarantees a minimum coolant flow output, maximum heater output temperature, and a minimum gas flow value to protect the heaters.

Different external devices support the proper operation of the CFV. The feeding system of the CFV allows the operation with different gases. This can be attained by modifying the gas bottle that is added to the system. Its standard operation consists of using dried air. This air is compressed by a set of compressors and then stored in high-pressure vessels. Next, the temperature of the air can be controlled by means of a power regulated electric heating system with maximum capacity of 30 kW. It is important to remark that the CFV structure is composed of several layers aimed at reducing the heat transfer to the environment. Finally, this device is designed to enable the application of simultaneous optical techniques. For this, it has three flat optical windows made by quartz, which allows no optical distortion. The main characteristics of the CFV vessel as well as the conditions used for the test are presented in Table 2.

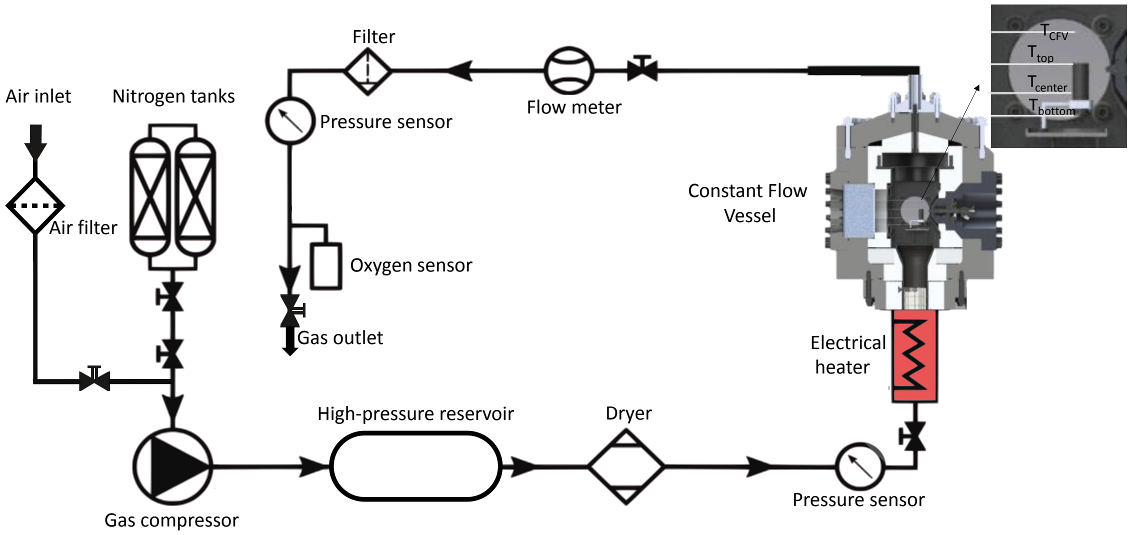

Figure 1 – Scheme of the experimental set up in the Continuous Flow Vessel (CFV).

Table 2 – Main test rig parameters for the battery thermal runaway study.

Parameter	Value
Thermocouples Type K, 1 mm diameter and 300 mm length, Range [°C]	Up to 1100
Volumetric flow meter, Brooks Models SLA5863S, Flow rate [l/min]	0-2000
Chamber pressure sensor, WIKA IS-20-S-BBP, Pressure range [bar]	0-160
Continuous Flow Vessel Messkammer CMT from Advanced Combustion GmbH, max pressure [bar] and max chamber temperature [°C]	150/1373
Control Volume Size [L]	40
Heating resistance power [kW]	30
Volumetric flow during experiment [m^3/h]	54
Pressure during experiment [bar]	2.6
Heating ramp for thermal abuse [°C/min]	11.0
Inlet gas [-]	Air/N_2

In this study, to investigate the thermal runaway occurrence at both inert and reactive conditions, the CFV was operated with the minimum allowable flow. This was found to be the best compromise between flame distortion and vessel scavenging in previous work [34]. A single heating ramp of 11^{o}C/min was considered for all the cases evaluated and was maintained for the whole analysis. This means that the heating device is never turned off during the experiment. The resistance power is controlled to maintain the 11^{o}C/min in the chamber temperature including after the thermal runaway episode to fully understand the cell behaviour in all the temperature range. This differs from the operation in accelerated rate calorimeters, which generally run on a heat-wait-search method. The higher heating levels also allows to decrease the experiment time in one order of magnitude compared to ARC and oven tests. In general, the total time spent during the evaluations is 25 min. More information about heating ramp effect can be seen in previous publication of the research group [34].

2.3. Optical techniques and experimental setup

The CFV contains three optical accesses, as shown in Figure 2. Two simultaneous optical techniques (Schlieren and Natural Luminosity) were employed during this investigation in the two optical accesses of 128 mm diameter located in a line-of-sight arrangement. The third window was replaced to include a thermocouple holder, which enabled to track the temperature evolution at different battery locations as well as in the interior of the CFV. A detailed description of the CFV can be found in previous works of the research group [34][35]. The Schlieren optical technique was applied aiming to visualize and characterize the venting of both gaseous and liquid phases. Additionally, the natural luminosity (NL) was recorded to investigate the combustion development through the thermal radiation emitted by the combustion process. Figure 2 illustrates the experimental setup used for this investigation, whereas Table 3 provides the most significant characteristics of the optical setup.

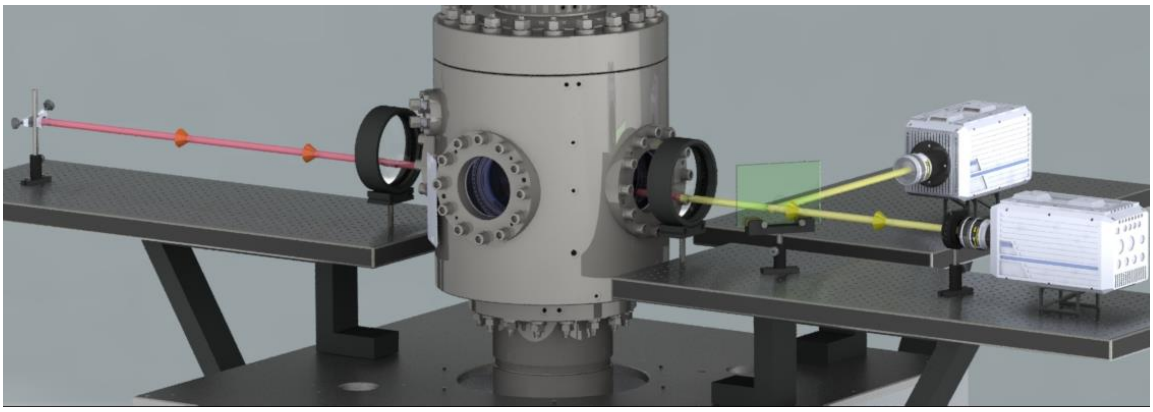

Figure 2 – Scheme of the optical techniques Continuous Flow Vessel (CFV).

Table 3 – Visualization components for Schlieren, Natural Luminosity and OH* tracking.

Component	Quantity	Specifications
High Speed Camera Photron Fastcam NOVA	*2*	*12-bit image, up to 16000 fps in max resolution.*
Lens Carl Zeiss Makro-Planar	*1*	*Focal length 100 mm, f/2 lens*
Lens Nikon UV	*1*	*Focal length 105 mm, UV, f/4.5 lens*
Beam splitter	*1*	*178x127 mm 50%T/50%R with a range from 450 to 750 nm.*
Light Source Karl Storz Nova 300	*1*	*Xenon lamp 300 Watts.*
Spherical lens	*1*	*f = 450 mm, D = 150 mm.*
Spherical UV lens	*1*	*f = 750 mm, D = 150 mm, UV.*
Iris diaphragm	*2*	*Metal iris diaphragm of diameter max 13 mm. Open diameter for experiment 5 mm.*

The refraction theory says that whenever a light ray that travels through a medium that has different refractive index gradients, it can suffer a deflection. This phenomenon is the basis of the Schlieren technique [36]. The same variation of refractive index can be found on density variations of a flow. Therefore, this phenomenon can be translated in as different grey levels in an image, allowing to observe the density field that is originated by the venting process. To obtain this, the light from the light source crosses the vessel from one window to the other and, consequently, trough the venting gases and liquids, which generates the Schlieren visualization. To visualize the vent gas and liquid ejected during the venting process, a high-speed single pass schlieren setup was developed. The illumination was attained by means of xenon lamp, driven with a liquid light guide. This allowed to create a point light source at the focal length plane of a spherical lens (f = 450 mm, D = 150 mm). In this sense, the area to be measured is illuminated with a collimated beam. The lens is separated from the light by 450 mm, while the CFV window and the lens are 5 mm apart. At the opposite side of the CFV, a spherical UV lens (f = 750 mm, D = 150 mm) was positioned near to the optical access (5 mm of the CFV window). The objective of this lens is to focus the light onto the Fourier plane where an iris diaphragm with a cut-off diameter of 5 mm was located. The UV lens and the iris diaphragm were separated by a distance of 750 mm. To quantify the process with values as the spray distance, speed penetration and spray angle, an image postprocessing was done by means of an in-house MATLAB code that is capable to subtract the background and define the spray contours by using a threshold of 60% of the maximum light. The penetration of the spray is quantified by the average distance of the further point of each jet during venting. The speed of the spray is calculated by derivation the spray penetration due to the temporal resolution of the images. Lastly, the cone angle is measured by the angle between opposite jets. The passage from pixel to millimetres is done with a spatial resolution calibration. As it is possible to observe, this calibration was checked with the diameter of the cell (18 mm).

Images were recorded at 12000 fps (0.083 ms) using a Photron Fastcam NOVA high speed CMOS camera close to the iris diaphragm. The camera was equipped with a Carl Zeiss Makro-Planar T 100 mm f/2 ZF2 camera lens (Carl Zeiss, Aalen, Germany). The shutter time was kept constant in 1.66 µs for all the experiments while the resolution was kept at 640 × 784 pixel with a total magnification of 6.8 pixel/mm. The combination of the frame rate and resolution gives a total recording time of 2.0 s. An end trigger was used to obtain the precise moment of the venting. Post processing of the images to calculate spray distance and speed penetration, as well as angle of the spray, was carried out in a MATLAB code. Details about the code and the assumptions used in the post processing such as the threshold levels are presented in a previous work [34].

The Natural luminosity signal has as source the thermal radiation emitted during the combustion process by the lithium ion cell [37]. This technique provides a way to investigate the propagation of the flame, its stabilization and quenching during the thermal runaway. This technique uses a Photron Fastcam NOVA high speed CMOS camera with an exposure time of 0.208 µs and a frame rate of 6000 fps (0.166 ms) was used. A Carl Zeiss Makro-Planar T 100 mm f/2 ZF2 lens was installed in the camera. The image resolution was 768x720 pixels with a spatial resolution of 6.6 pixels/mm. This camera was positioned in perpendicular to the field of view as shown in Figure 2. A beam splitter is used to reflect the light to the camera which is manually triggered to record images from the start of the combustion.

3. Results

The results section is divided into two different parts. First, the thermodynamic results are presented, illustrating the effect of the different battery chemistries and environmental conditions on the temperature evolution and characteristic parameters of the thermal runaway process. Finally, the optical results from the schlieren and natural luminosity in the venting and combustion process are discussed in detail.

3.1. Thermodynamic Results

Six experimental tests were done with three battery chemistries and two oxygen concentrations in the continuous flow chamber (21% and 0%). Figure 3 shows the temperature evolution comparison for the same battery chemistry with Air (21% O_2) and N_2 (inert condition, 0% O_2). The sensor located in the chamber shows the temperature evolution of the ambient that surrounded the battery cell and the cell temperature sensor shows the average temperature of three sensors located in the center and extremes of the cylindrical cell. Figure 3a and Figure 3b shows the LCO (Samsung 26J) cell in which is possible to observe that the instant of initiate the TR as well as the venting is similar between air and N_2. The first phenomenon is identified by a suddenly increase of temperature with a peak above 300ºC in the chamber and cell and the second phenomenon by a small decrease of surface temperature of the cell before the TR. Both processes will be described in the image section analysis with more details. Initially, it can be observed that the thermal runaway temperature onset is maintained, independently on the atmosphere that is used outside of the battery. This result agrees with the phenomenological explanation of the thermal runaway, where the main driver is attributed to the temperature increase. External temperatures may modify the heat transfer rate from the battery to the environment and vice-versa. But, since the temperature is maintained during the heating phase for both cells, the heat transfer phenomena is not very much dominant on the early phases of the TR. During the thermal runaway evolution, the case with air (oxygen presence) achieves a higher chamber peak. Both cases show a similar temperature increase in the first instant, but the inert case had a higher temperature cell along all the TR process. The maximum internal temperature achieved during the thermal runaway is dependent on several factors. First, the SOC of the battery dictates the amount of intercalated lithium-ion that are charged (reactive mass) and may react during the thermal runaway. In addition, the venting process dictates the quantity of mass that is released in the early phases of the battery decomposition. Since this mass is expelled to the environment, it will not contribute to the internal temperature increase. State-of-charge differences are discarded in this case, since each of the cells were conditioned by means of a rigorous process using charge controller devices. In this sense, the differences observed in the temperature evolution might be related to the amount of mass that remains inside the battery during the thermal runaway as well as the heat transfer from the cell to the environment for high temperature conditions, i.e., conditions were the CFV temperature is modified by the TR. The former is hypothesized to be the most relevant parameter in this case, since the CFV temperature profiles does not demonstrates any direct behavior with what is seem in the cell temperature. It is evident that the mass expelled during the thermal runaway occurrence cannot be assured to be the same from cell-to-cell experiments, since the main driver of the mass flow (pressure gradient) is a consequence of the geometry of the nozzles, the rupture of the safety disk, the deposition of material along the nozzles, etc. In this sense, it is believed that the modifications of the environment conditions and the avoidance of flame outside of the cell, could be a factor that influenced the release of mass from the battery to the environment during the high temperature phase of the thermal runaway. It is important to notice that the battery cell was heated with a constant heat ramp of 11°C/min until the TR finish. This means that the cell temperature reaches the chamber temperature after the suddenly increase.

Similar investigation was done for the NMC (Samsung 20R) and the LFP (NX9073). Figure 3c and Figure 3d shows that the venting was seen at similar time for both cases, but the TR was first for the oxygen content case. Despite the cell temperature peak was close for both conditions, the chamber temperature was 2 times higher for the air case than in inert conditions as seen for the NMC cell. The increase of the temperature of the environment due to the combustion of the expelled gases modifies the conditions for heat transfer from the cell to the environment. In this scenario, the Newton cooling law results in a deteriorated heat transfer from the cell to the environment, requiring more time to transfer the heat generated inside the battery to the environment and also resulting in higher peak temperatures. This is also subjected to the assumptions made for the LCO chemistry (same quantity of vented gases). Lastly, the LFP was the cell with more variation between both ambient conditions (Figure 3e and Figure 3f). The TR starts first for the air case and the cell peak temperature was higher than inert case. However, the most noticeable difference with the other presented cases is the chamber temperature similar for both cases. This will be explained in the next section due to the presence or not of flame in the top of the battery cell.

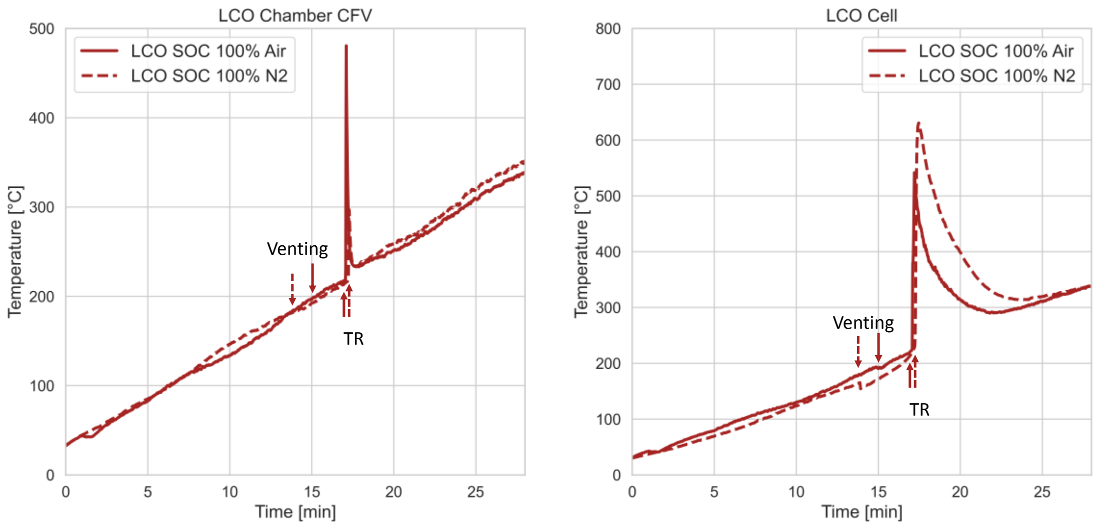

(a) (b)

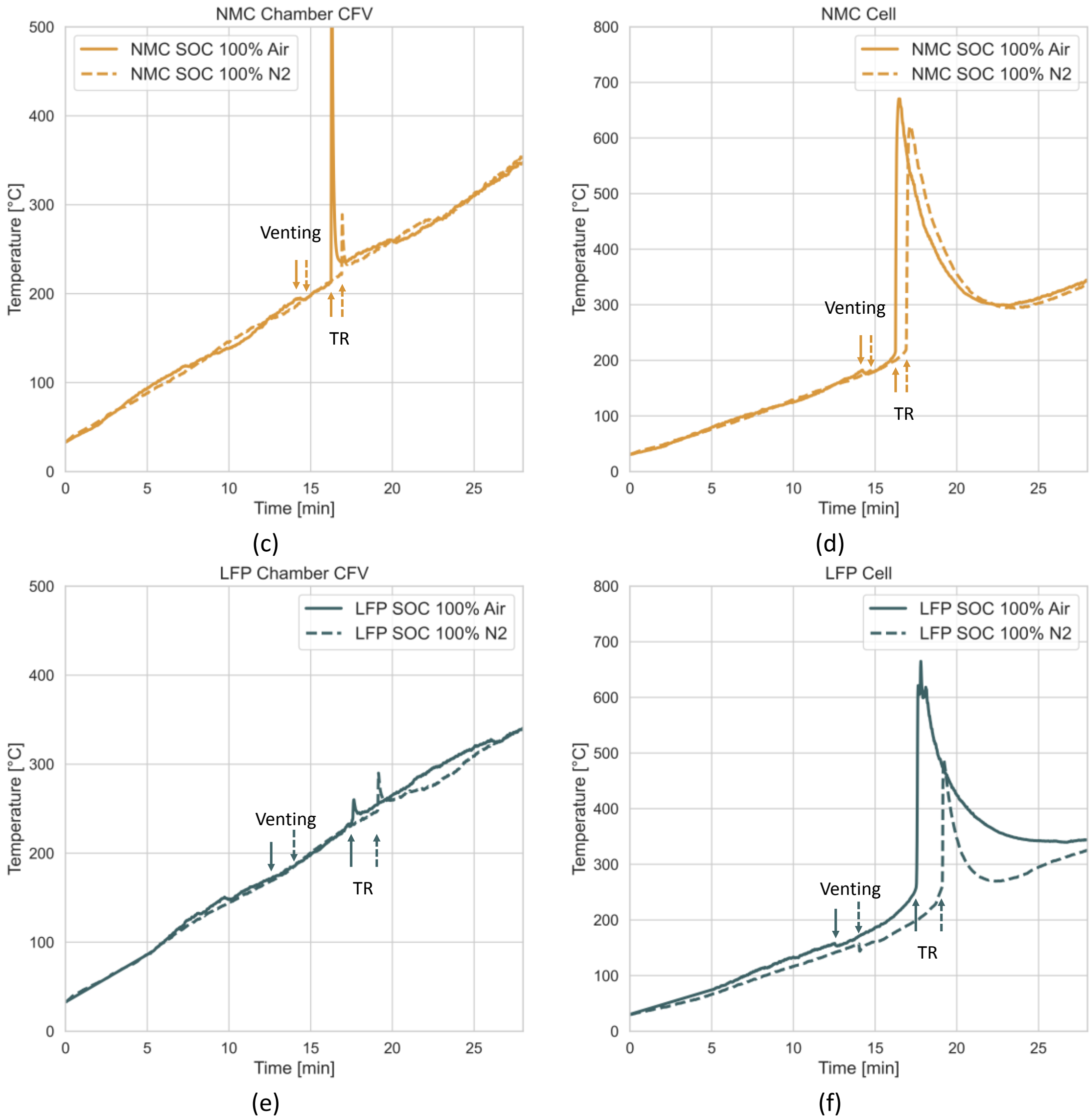

Figure 3 – Comparison between Air and inert N_2 atmosphere for three cell chemistries. Continuous flow vessel (CFV) chamber temperature and battery cell temperature for a heating ramp of 11.0°C/min.

To better understand the differences between chemistries, Figure 4 depicts the previous temperature profiles but compared by cell type in the same ambient conditions. This graph allows to observe that the NMC is the first cell to enter in TR, followed by the LCO and lastly the LFP. This result concurs with the observations from Yuan et al. [23] and it is attributed to the intrinsically stable nature of Fe and the low oxygen generation by the cathode decomposition. Also, the peak temperature follows the same trend when the chamber sensor is seen. For the cell average temperature, the maximum value is similar between NMC and LFP and a slightly lower for the LCO. Despite the delayed TR for the LFP, it is the first cell in venting followed by the LCO and NMC. This means that the LFP has the largest safety time (defined as time between venting and TR).

For the inert case, the NMC and LCO shows similar TR trend with close time event and peak temperature on the chamber and cell surface. The LFP shows, as in the O_2 content case, a delay in the TR and an early venting with respect to the Samsung LCO and NMC cells. The chamber and average cell temperature were lower than the other two chemistries. This confirms that for both ambient scenarios the LFP shows the highest safety time and lower ambient temperature. For a safety perspective, this is a positive point due to the impact that this may have on other cells, battery case and prevention system.

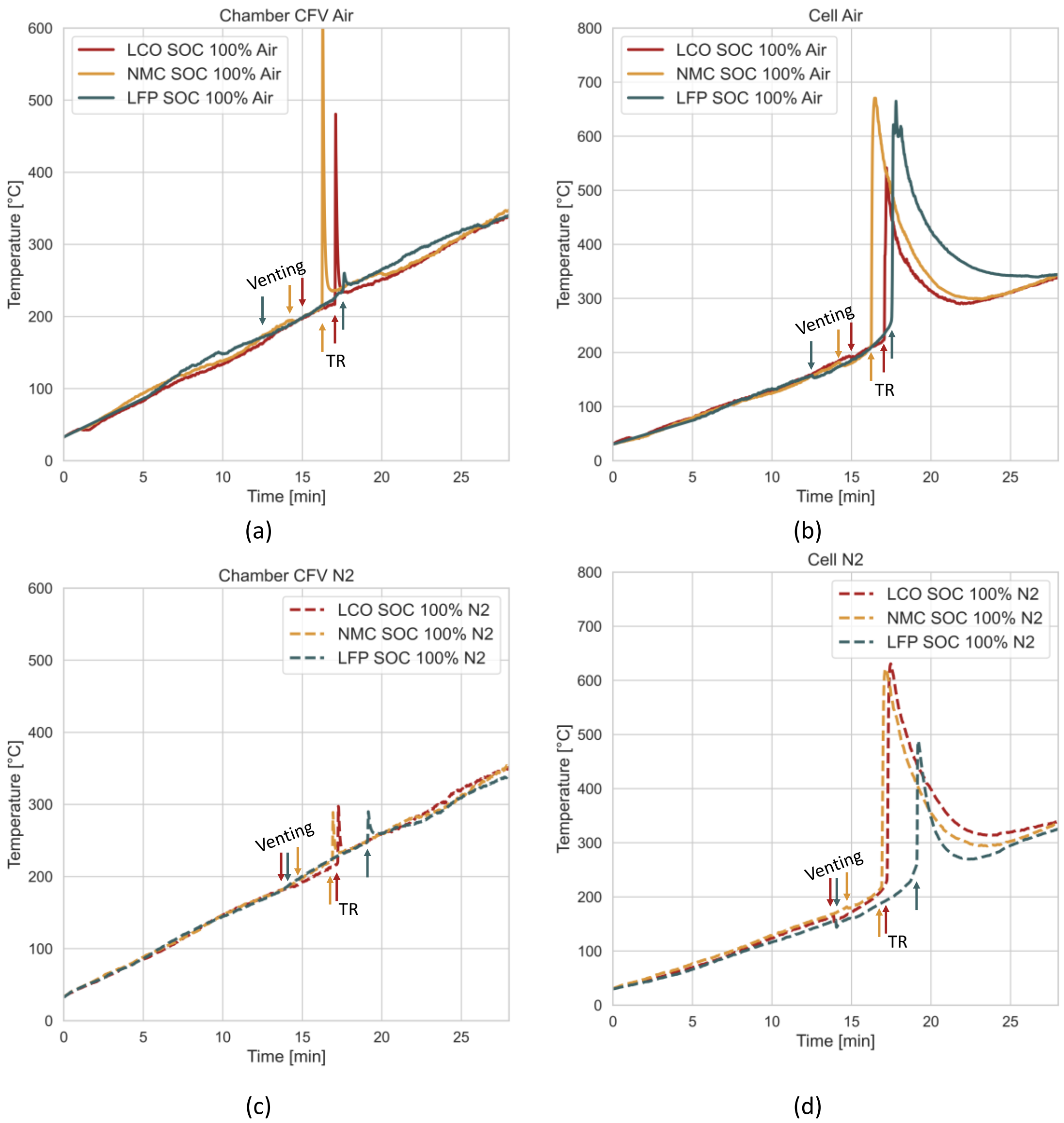

Figure 4 – Comparison between cell chemistries when is tested with Air and inert N_2 atmosphere. Continuous flow vessel (CFV) chamber temperature and battery cell temperature for a heating ramp of 11.0°C/min.

The details of the main significative parameters of the venting and TR seen in Figure 4 (previous) are summarized in Figure 5 and Figure 6. These figures are interesting since they allow to identify both processes in terms of temperature and time. For the three cells, the average venting temperature was 173°C with a standard deviation of 14°C. Separating in air and N_2, the average values are 178°C and 167°C, respectively, with a similar standard deviation around 11°C. Focusing on the battery chemistry, the LCO, NMC and LFP shows: 179°C, 182°C and 157°C, respectively. Observing the battery chemistry in both ambient conditions the standard deviation is drastically reduced below 2°C. The case that did not reduce this variation is the LCO with 15°C. Despite the LCO shows different trend, the ambient conditions do not have a strong influence in the moment and temperature that the venting is produced. The main change is the battery chemistry.

The smoke event, which marks the start of the thermal runaway shows average values of 230°C and 236°C for air and N_2, respectively, with a similar standard deviation around 18°C. Focusing on the battery chemistry, the LCO, NMC and LFP shows smoke at: 227°C, 214°C and 257°C, respectively. As was seen for the venting, the battery chemistry is the most influencing parameter due to the drastically reduced of the standard deviation below 4°C for the three cases.

These results are strongly influenced by the cathode layering and composition and by the cell manufacturing. The former promotes the stability of the cell, as previously referred in this section. For example, the addition of Fe in the cathode layer provides much higher stability than low Cobalt chemistries such as NMC and NCA. This dictates the onsets of the battery thermal runaway, i.e., the temperatures where the exponential temperature increase is realized. Nonetheless, another important battery feature needs to be accounted in these comparisons. Each battery cell is unique in terms of safety vent cap production since it is not possible to assure an exactly equal production process. Moreover, each cathode chemistry can have its own vent cap opening pressure. This seems to be the case, for example, for the LFP chemistry, where the first venting event is evidenced much earlier in temperature compared to the NMC and LCO, despite being a much stable cathode chemistry. The proper definition of the vent cap opening pressure requires dedicated experiments and instrumentation and will be introduced in future investigations.

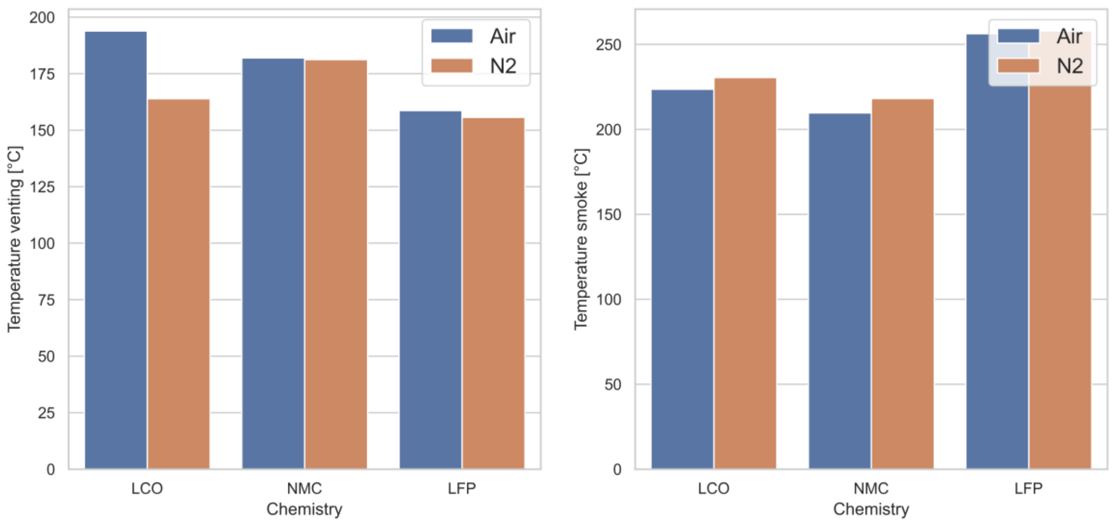

(a) (b)

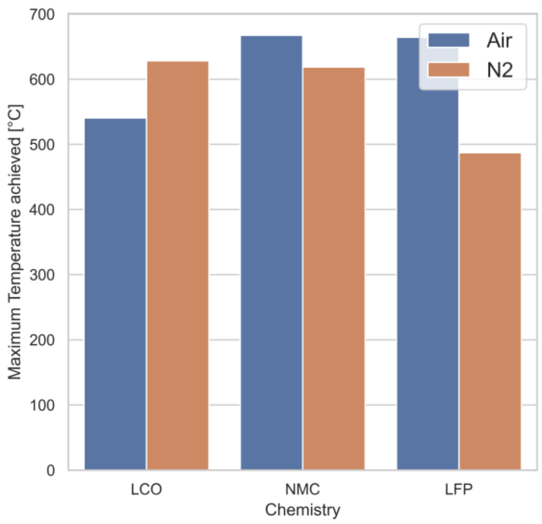

(c)

Figure 5 – Main parameter of thermal runaway by thermal abuse in terms of temperature measured in the battery cell.

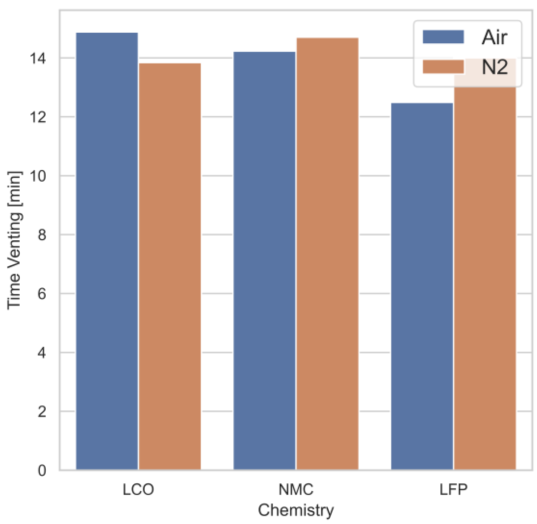

(a)

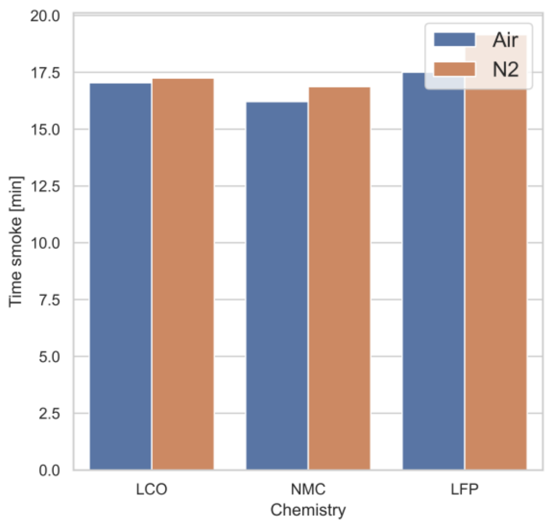

(b)

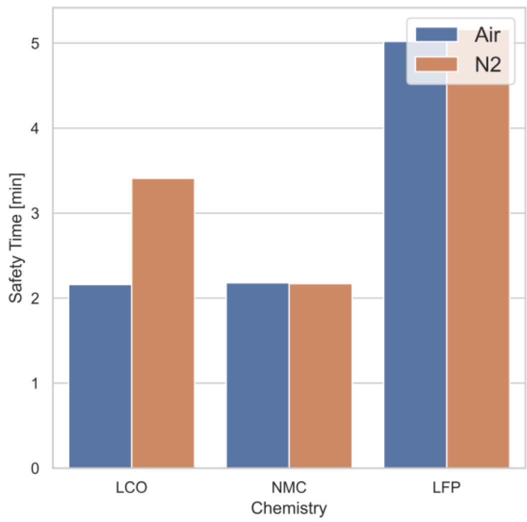

(c)

Figure 6 – Main parameter of thermal runaway by thermal abuse in terms of time measured in the battery cell.

3.2. Visualization results

The visualization section is separated in two parts due to the two main events during the battery thermal abuse. The first event is the venting of the liquid electrolyte and all gases generated by the decomposition of the different layers. In the thermodynamic analysis, it was seen a decrease of the battery surface temperature of around 5ºC without any relevant change in the chamber temperature measurement. The second event is the thermal runaway, seen in the previous analysis as a self-heating phase where the battery cell temperature increases progressively until a suddenly increase of the temperature. A peak is reached in both, the cell, and the chamber, followed by a cooling phase of the battery cell with the ambient temperature that continues increasing with the heating ramp set.

Based on a previous work of the research, group [34], during the venting process both liquid and gas are expected to be released by the venting cap . Therefore, the Schlieren technique is applied as shown in the methodology. On the other hand, on the thermal runaway is generally seen a flame formed in the surrounding of the cell due to the fuel gases and the hot temperature of the chamber and cell surface. Therefore, the natural luminosity optical technique is applied to identify the flame growth and development along the event. To observe the smoke formation that can be found in some battery chemistries, the light of the schlieren was maintained. Therefore, in the camera of NL the smoke will be identify as an attenuation of this light.

Venting Process

The venting process was captured by means of the Schlieren technique for the 6 cases (three chemistries and two oxygen contents). Figure 7 shows the first 4 ms since is possible to see any ejection of liquid or gas. The frame rate used was 12,000 fps (0.0833 ms). Therefore, as the time step used in Figure 7 is 0.5 ms, there are 5 figures between each figure showed below. This is mentioned to show the accuracy of the first instant that is possible to see the venting of cell component. For the brevity of the manuscript, all figures can be seen in the video on the supplementary material. From a qualitative point of view, in Figure 7 it is possible to observe that the LCO have a wider spray cone with more visible jets. This is mainly due to the double number of holes (six holes) than the other two cells (3 holes). Due to the camera position, in the six holes vent cap of the LCO is only possible to see three clear jets. For the other cells, NMC shows clear two jets and the LFP in the beginning only on jet but after 2.5 ms is divided into three jets. After the test ends, it is possible to see that the vent cap rupture obstructs one hole. This explains the two visible jets.

Furthermore, for the same cell chemistry in different ambient conditions, the spray have large changes. As the properties of gas density, diffusivity among other is close for Air and pure N_2, the variation can be more related to the venting process and the cell behaviors. The vent cap rupture in an irregular way can influence in the ejection of the liquid, gas and, in less quantity, solid parts of the battery cell. In the first 4 ms it is possible to see a large amount of liquid being released together with gases. This can be appreciated for the dark color of the images instead of a simple grey variation when is only gas detected.

Figure 8 shows a sequence with 400 ms with a time step of 50 ms for better appreciate all venting process. The LFP shows large time of liquid ejection with higher droplets size for both air and N_2 cases. On the other hand, the NMC was the first to finish the combined liquid-gas phase to continue only with gas ejection. After the 400 ms, all cells continue ejecting gas but with low intensity until the thermal runaway.

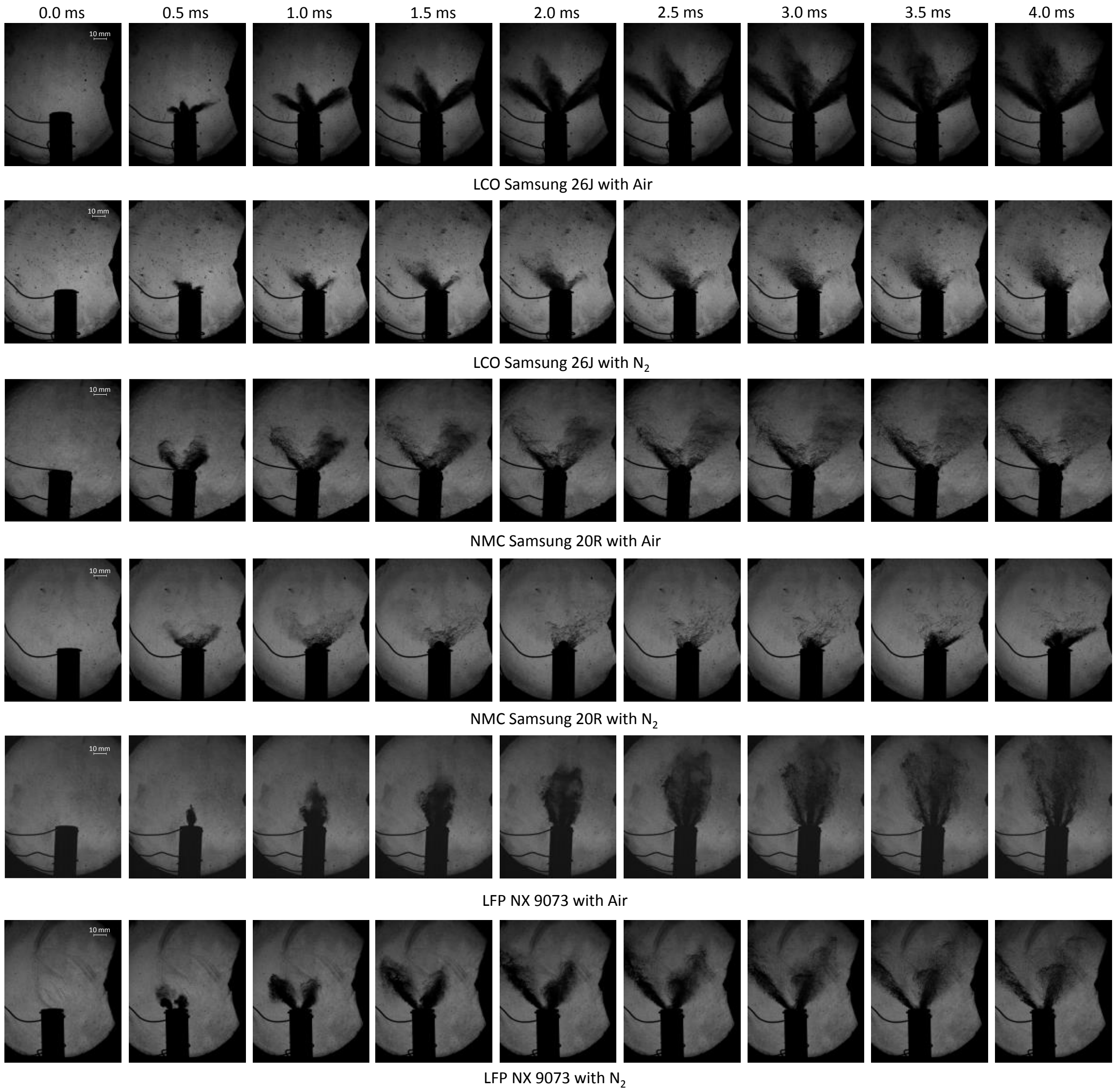

Figure 7 –Schlieren Technique for venting process with 0.5 ms of step time.

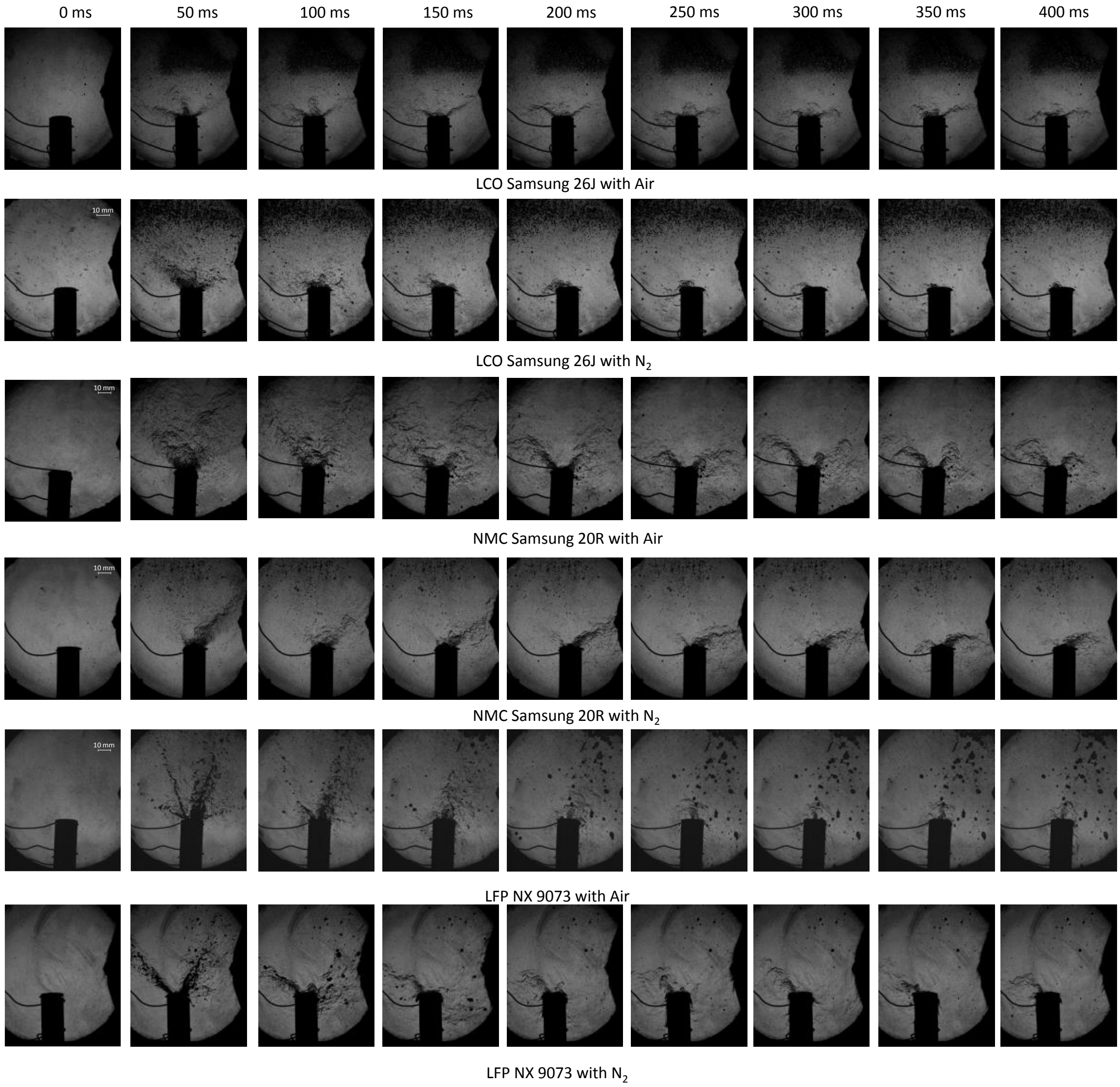

Figure 8 –Schlieren Technique for venting process with 50 ms of step time.

Figure 9 shows a quantitative analysis of the first instant of the venting process in which there is no wall interaction, and the ejection is mainly liquid phase for the three chemistries with air. The results shown in Figure 9a are the average of the jet distance from the vent cap center as well the speed derivative from the last measured parameter. The NMC has the fast growth in the beginning of the process (until 1 ms) with a peak speed of 50 m/s instead of 30 m/s for the LCO and LFP, but after 3 ms the trend is reverted. The NMC starts to have less ejected liquid. Therefore, the spray starts to decrease while for the LCO and LFP the spray is maintained. The other interesting parameter is the cone defined as the angle between the left and right jet (Figure 9b). The results show that LCO start with a wide angle and after 3 ms the three jets are closer with a constant angle around 110^o. The NMC with two jets maintains an angle around 85^o for the entire process. Lastly, the LFP spray cone angle graph shows that start the three jets close to the vertical axis and then it opens with the three jets making a cone of 50^o. It is possible to observe that despite the NMC and LFP have three holes the spray is different due to the fabricant design, vent cap rupture and liquid content.

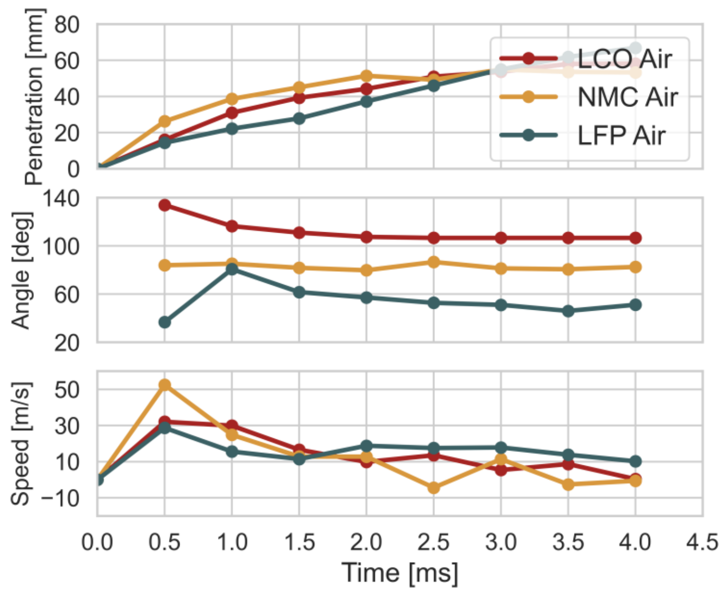

Figure 9 –Schlieren Technique for venting process with 50 ms of step time in terms of average jet distance from the vent cap, angle between right and left jets (cone angle) and average speed obtained from the measured distance.

Combustion Process

After the venting process seeing in the previous section, it exists a period of self-heating until the point that the cell enters in thermal runaway. In the thermodynamic analysis can be seen as a suddenly increase of the temperature with the cell surface up to 700ºC and chamber up to 500ºC. This section shows the thermal runaway with a natural luminosity technique taken with a frame rate of 6000 fps. As it was mentioned in the methodology, the light source is maintained for the smoke visualization.

Figure 10 shows the six cases with a time step of 100 ms to observe almost one second of the thermal runaway process. The LCO and NMC cells in air environment show flame propagation from the vent cap. Despite being a continuous flow, the gas and temperature were enough high for the combustion ignition and maintenance. The LCO did not show smoke period and the flame propagates in the same three jets observed during the venting process (see Figure 7). The NMC did not show a clear preferential flame propagation, being all around the vent cap. The other information that can be obtained is that to perform a spatial characterization, as was done with the spray during the venting process, is not an easy task. The flame has random propagation with changes due to the inlet CFV gas and gas flow from inside the battery. For the LCO, the flame is sustained in three clear jets. However, the NMC shows a not defined flame with part being downstream.

The main different behaviour was seen in the LFP, which in presence of oxygen did not show flame. For this cell, the smoke is less intense than the inert case. In addition, a characteristic of this test is that the vent cap was totally ruptured and the interior of the cell was expulsed to the outside. The reader is invited to see the supplementary material to observe the final state of the cell.

The inert cases (no oxygen content) did not show flame. Despite several studies show that the vent gas contains oxygen, but it is not enough for the flame ignition. All cells show an intense smoke generation with difficulties to observe the cell after 500 ms. This drops the conclusion that using a battery package without air content inside can be a good alternative to avoid flame propagation. However, the temperature increase cannot be avoided with inert atmosphere as shown in the thermodynamic analysis. For the three cells, the smoke is intense and cannot be removed easily in spite of the high CFV volumetric flow of inlet gas.

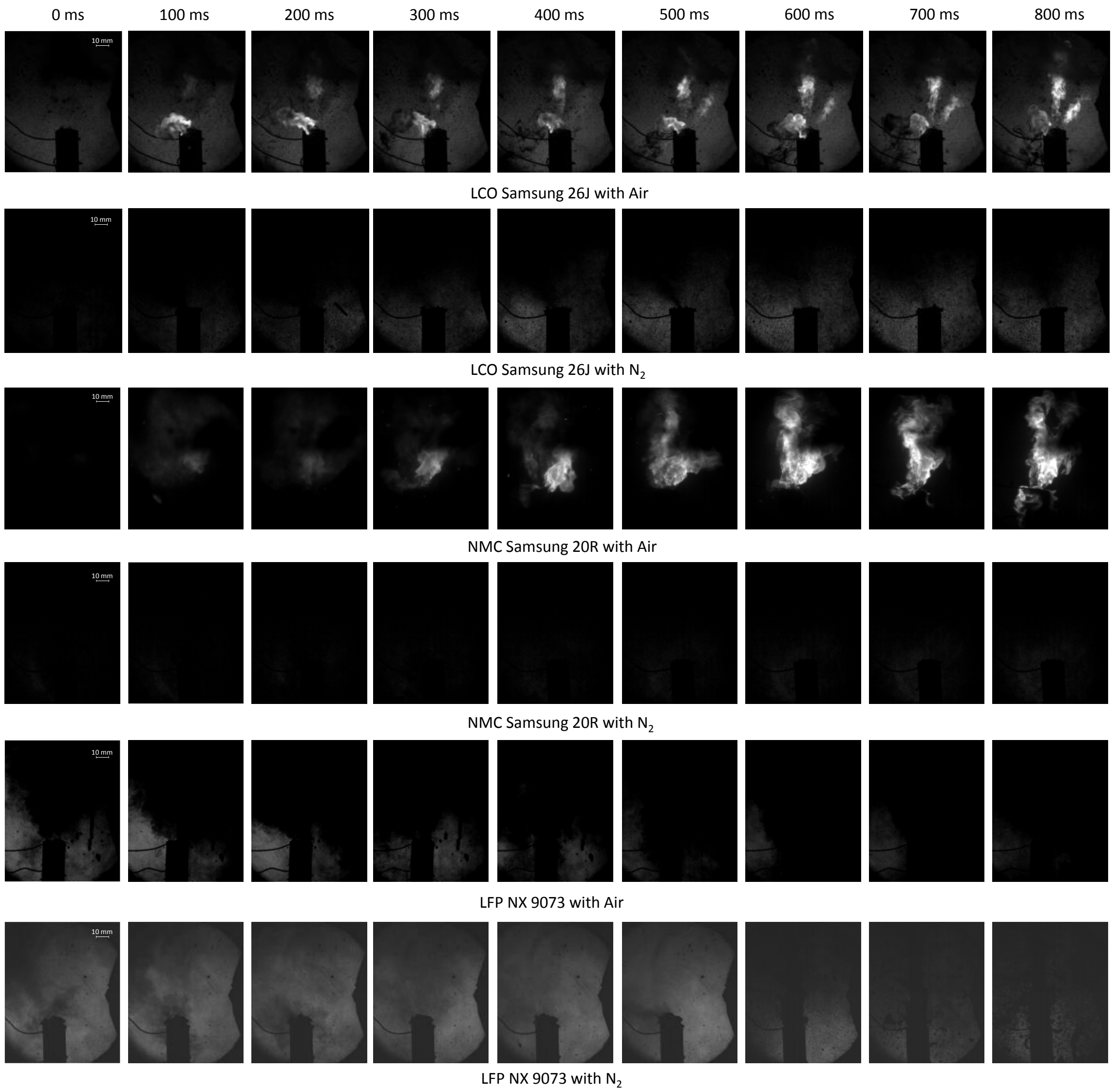

Figure 10 – Natural Luminosity during thermal runaway with 100 ms of step time.

Lastly, Figure 11shows the mass loosed of each cell during the experiment. The mass is loosed in the venting process due to the material expulsion, gas generation by the chemical reaction and liquid expulsion. In addition, the thermal runaway additional mass is loosed. These values are calculated by difference between the mass cell before and after the experiment by a high precision scale. Figure 11 depicts that the main difference was seen for LFP in air content. The images shows that the venting is like the case in inert condition, but the smoke event and absence of fire will end in a less amount of mass loosed. For the others cases the mass loss is similar with around 43% of the initial mass.

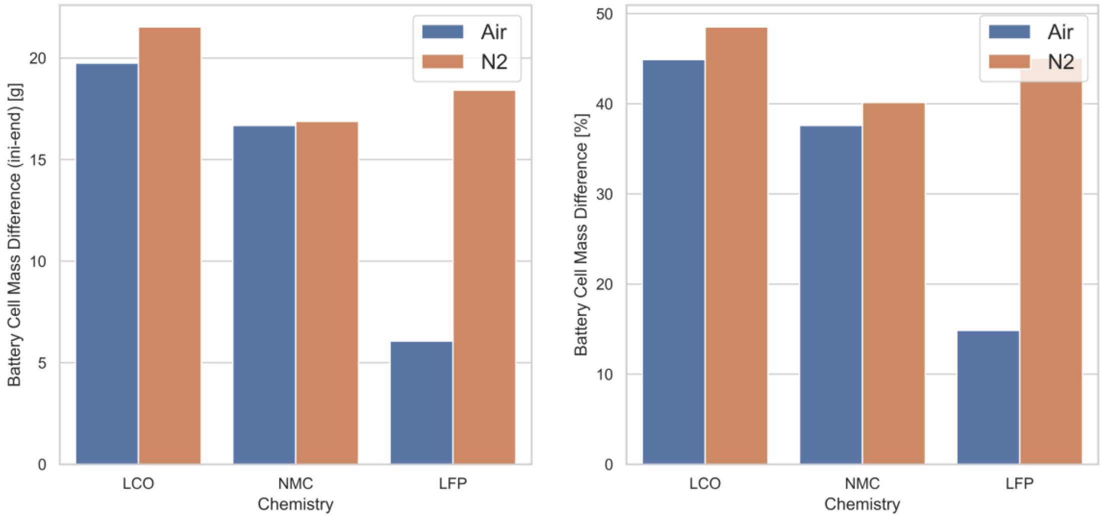

(a) (b)

Figure 11 – Mass difference after and before the test (a). The mass percentage loss (b) is calculated as the mass difference divided by the initial mass. The graphs present the results for LCO, NMC and LFP batteries in Air and N_2.

4. Conclusion

This study analysed the behaviour of different commercial 18650 lithium-ion cells in inert and air atmosphere in a continuous flow vessel. The cells were heated with a constant ramp of 11.0°C/min until the thermal runaway occurrence. Different thermocouples were attached to the cell surface as well as the chamber. An optical set up was used for the venting and combustion record during the cell heating. The combination of both thermodynamic and optical analysis has allowed to obtain interesting insights considering both the different cathode chemistries and CFV environments. The main conclusions can be summarized as:

Cathode Chemistry:

- The NMC showed the fastest spray with top speed of 50 m/s in the first 1 ms while rapidly reduce the amount of liquid and gas ejected compared to the LCO and LFP. In addition, for this cell only two jets of the three holes could be saw.
- The LCO and LFP showed similar initial speed 20 m/s and maintained a constant speed of around 12 m/s until 4 ms. After that, the speed starts to decrease and

from this point until the thermal runaway, the gas ejection occurred in a low proportion.

- The safety time measurements show that LFP allows for up to 5 min compared to the NMC, which showed only 2 min of safety time.
- The LCO showed a variation of 1.1 min between the air and inert cases with an average safety time of 2.7 min. The venting was produced after 13 min of heating and the thermal runaway vary from 17 to 19 min after the experiment starts.

Environmental condition:

- In the cases with air, the LCO and NMC showed a high increase of the temperature chamber gas (increase of 300°C), while for LFP was only around 50°C.
- The optical technique allowed to identify this difference by the absence of fire in the case of LFP. The inert atmosphere prevented the fire. Other studies show that the vent gas has oxygen as part of the gas composition. However, from the results of this investigation, it could be concluded that the oxygen released from the cell inside is not enough to initiate the combustion process.
- Despite not having external combustion, the cell surface temperature is still high for the N_2 environment, reaching levels comparable to the air atmosphere cases.

The individual observations allow to conclude that the absence of reactive environment outside the battery cells offers an effective pathway to supress the combustion initiation of the vented gas. This does not offer only a way of reducing the damage of the battery case but also reduces the heat transfer from the battery entering in thermal runaway to those of the vicinity by both convective and radiative heat transfer. This certainly offers an edge on avoiding the progressing of the thermal runaway process to other cells. Finally, the use of inert atmospheres also allows to extend the venting and smoke times, providing extra opportunities for system actuation and for leaving the vehicle.

Future studies will focus on studying the gas and liquid composition of the vent gas as well as a spectroscopy optical technique to understand the chemical species generated in the thermal runaway when oxygen is present in the atmosphere."

Abbreviations

LFP	Lithium *Ferrum* Phosphate	ICR	Lithium Cobalt Rechargeable
BEV	Battery Electric Vehicles	LCO	Lithium Cobalt Oxide
BTR	Battery Thermal Runaway	Li	Lithium Ferrum Phosphate
C.V	Control Volume	mm	Millimeter
CFV	Continuous Flow Vessel	ms	Millisecond
deg	Degree	NCA	Nickel Cobalt Aluminium Battery Cell Cathode Material
f	Focal Length	NL	Natural Luminosity
f/	Focal Number	nm	Nanometer
fps	Frame Per Second	NMC	Nickel Manganese Cobalt Battery Cell Cathode Material

Gr	Graphite	OH*	OH Radical
Gr+SiOx	Graphite And Silicon Oxide Composite	S	Sulphur
ICCD	Intensified Charged-Coupled Device	SEI	Solid Electrolyte Interface
ICE	Internal Combustion Engine	UV	Ultra Violet
ICEVs	Internal Combustion Engine Vehicles		

5. Acknowledgments

The authors want to acknowledge: Operación financiada por la Unión Europea a través del Programa Operativo del Fondo Europeo de Desarrollo Regional (FEDER) de la Comunitat Valenciana 2014-2020 con el objetivo de promover el desarrollo tecnológico, la innovación y una investigación de calidad. As well as the: Proyecto IDIFEDER/2021/053, Equipamiento para el estudio del fenómeno de combustión no controlada en baterías de vehículos eléctricos, entidad benificiaria Universitat Poliécnica de Valéncia. Lastly: Proyecto IDIFEDER/2020/34, EQUIPAMIENTO PARA EL DESARROLLO DE PLANTAS PROPULSIVAS HÍBRIDAS LIMPIAS Y EFICIENTES A TRAVÉS DEL USO DE E-FUELS, entidad beneficiaria Universitat Politècnica de València.

6. References

[1] E. Environmental and G. Governance, “Editorial Policy Contents Message from the Head of the Company Overview of Toyota Motor Corporation Changes in Key Consolidated Financial Data Editorial Policy This Environmental Report is a part of the Sustainability Data Book and reports on Toyota ’ s “,” p. 42, 2020.

[2] EPA, “The 2020 EPA Automotive Trends Report,” *Epa*, no. March, pp. 1–12, 2020.

[3] THE INTERNATIONAL COUNCIL ON CLEAN TRANSPORTATION, “2020 – 2030 CO 2 standards for new cars and light-commercial vehicles in the European Union,” *Icct*, no. November, 2016.

[4] I. panel on climate Change, “Climate change 2021:the physical science basis,” 2021.

[5] The European Comission, “REGULATIONS. Commission regulations (EU) 2019/318 of February 2019 amending Regulation (EU) 2017/2400 and Directive 2007/46/EC of the European Parliament and of the Council as regards the determination of the CO2 emission and fuel cunsumption of heavy-dut,” *Off. J. Eur. Union*, vol. 2001, no. May, pp. 20–30, 2019.

[6] European Environment Agency, “Emissions of air pollutants from transport,” *Indic. Assess.*, p. 12, 2018.

[7] S. Wappelhorst, “The end of the road? An overview of combustionengine car phase-out announcements across Europe,” *Int. Counc. Clean Transp.*, no. May, pp. 1–19, 2020.

[8] A. Nordelöf, M. Romare, and J. Tivander, “Life cycle assessment of city buses

powered by electricity, hydrogenated vegetable oil or diesel," *Transp. Res. Part D Transp. Environ.*, vol. 75, no. September, pp. 211–222, 2019.

[9] C. X. He, Q. L. Yue, M. C. Wu, Q. Chen, and T. S. Zhao, "A 3D electrochemical-thermal coupled model for electrochemical and thermal analysis of pouch-type lithium-ion batteries," *Int. J. Heat Mass Transf.*, vol. 181, p. 121855, 2021.

[10] N. Wu, X. Ye, J. Yao, X. Zhang, X. Zhou, and B. Yu, "Efficient thermal management of the large-format pouch lithium-ion cell via the boiling-cooling system operated with intermittent flow," *Int. J. Heat Mass Transf.*, vol. 170, p. 121018, 2021.

[11] W. Yan, Z. Wang, and S. Chen, "Quantitative analysis on the heat transfer modes in the process of thermal runaway propagation in lithium-ion battery pack under confined and semi-confined space," *Int. J. Heat Mass Transf.*, vol. 176, p. 121483, 2021.

[12] J. Liang, Y. Gan, M. Tan, and Y. Li, "Multilayer electrochemical-thermal coupled modeling of unbalanced discharging in a serially connected lithium-ion battery module," *Energy*, vol. 209, p. 118429, 2020.

[13] L. He *et al.*, "Structure optimization of a heat pipe-cooling battery thermal management system based on fuzzy grey relational analysis," *Int. J. Heat Mass Transf.*, vol. 182, 2022.

[14] W. Mei, H. Li, C. Zhao, J. Sun, and Q. Wang, "Numerical study on thermal characteristics comparison between charge and discharge process for lithium ion battery," *Int. J. Heat Mass Transf.*, vol. 162, p. 120319, 2020.

[15] Z. An, L. Jia, L. Wei, and C. Yang, "Numerical modeling and analysis of thermal behavior and Li+ transport characteristic in lithium-ion battery," *Int. J. Heat Mass Transf.*, vol. 127, pp. 1351–1366, 2018.

[16] C. Liu, H. Li, X. Kong, and J. Zhao, "Modeling analysis of the effect of battery design on internal short circuit hazard in LiNi0.8Co0.1Mn0.1O2/SiOx-graphite lithium ion batteries," *Int. J. Heat Mass Transf.*, vol. 153, p. 119590, 2020.

[17] T. D. Hatchard, D. D. MacNeil, A. Basu, and J. R. Dahn, "Thermal Model of Cylindrical and Prismatic Lithium-Ion Cells," *J. Electrochem. Soc.*, vol. 148, no. 7, p. A755, 2001.

[18] D. Ren *et al.*, "An electrochemical-thermal coupled overcharge-to-thermal-runaway model for lithium ion battery," *J. Power Sources*, vol. 364, pp. 328–340, 2017.

[19] D. Ren *et al.*, "Model-based thermal runaway prediction of lithium-ion batteries from kinetics analysis of cell components," *Appl. Energy*, vol. 228, no. June, pp. 633–644, 2018.

[20] Y. S. Duh *et al.*, "Characterization on thermal runaway of commercial 18650 lithium-ion batteries used in electric vehicles: A review," *J. Energy Storage*, vol. 41, no. May, p. 102888, 2021.

[21] S. Zheng, L. Wang, X. Feng, and X. He, “Probing the heat sources during thermal runaway process by thermal analysis of different battery chemistries,” *J. Power Sources*, vol. 378, no. July 2017, pp. 527–536, 2018.

[22] A. García, J. Monsalve-Serrano, R. Lago Sari, and Á. Fogué Robles, “Numerical analysis of kinetic mechanisms for battery thermal runaway prediction in lithium-ion batteries,” *Int. J. Engine Res.*, p. 146808742110299, 2021.

[23] L. Yuan, T. Dubaniewicz, I. Zlochower, R. Thomas, and N. Rayyan, “Experimental study on thermal runaway and vented gases of lithium-ion cells,” *Process Saf. Environ. Prot.*, vol. 144, pp. 186–192, 2020.

[24] M. Chen, J. Liu, D. Ouyang, and J. Wang, “Experimental investigation on the effect of ambient pressure on thermal runaway and fire behaviors of lithium-ion batteries,” *Int. J. Energy Res.*, vol. 43, no. 9, pp. 4898–4911, 2019.

[25] L. S. Guo, Z. R. Wang, J. H. Wang, Q. K. Luo, and J. J. Liu, “Effects of the environmental temperature and heat dissipation condition on the thermal runaway of lithium ion batteries during the charge-discharge process,” *J. Loss Prev. Process Ind.*, vol. 49, pp. 953–960, 2017.

[26] J. Weng *et al.*, “Alleviation on battery thermal runaway propagation: Effects of oxygen level and dilution gas,” *J. Power Sources*, vol. 509, no. August, p. 230340, 2021.

[27] X. Yang *et al.*, “An Experimental Study on Preventing Thermal Runaway Propagation in Lithium-Ion Battery Module Using Aerogel and Liquid Cooling Plate Together,” *Fire Technol.*, vol. 56, no. 6, pp. 2579–2602, 2020.

[28] A. O. Said, C. Lee, S. I. Stoliarov, and A. W. Marshall, “Comprehensive analysis of dynamics and hazards associated with cascading failure in 18650 lithium ion cell arrays,” *Appl. Energy*, vol. 248, no. April, pp. 415–428, 2019.

[29] A. O. Said, C. Lee, and S. I. Stoliarov, “Experimental investigation of cascading failure in 18650 lithium ion cell arrays: Impact of cathode chemistry,” *J. Power Sources*, vol. 446, no. November 2019, p. 227347, 2020.

[30] J. Wang, Y. Gan, J. Liang, M. Tan, and Y. Li, “Sensitivity analysis of factors influencing a heat pipe-based thermal management system for a battery module with cylindrical cells,” *Appl. Therm. Eng.*, vol. 151, no. January, pp. 475–485, 2019.

[31] J. Liang, Y. Gan, and Y. Li, “Investigation on the thermal performance of a battery thermal management system using heat pipe under different ambient temperatures,” *Energy Convers. Manag.*, vol. 155, no. August 2017, pp. 1–9, 2018.

[32] R. Payri, J. S. Giraldo, S. Ayyapureddi, and Z. Versey, “Experimental and analytical study on vapor phase and liquid penetration for a high pressure diesel injector,” *Appl. Therm. Eng.*, vol. 137, no. March, pp. 721–728, 2018.

[33] R. Payri, F. J. Salvador, R. Abboud, and A. Viera, “Study of evaporative diesel spray interaction in multiple injections using optical diagnostics,” *Appl. Therm.*

Eng., vol. 176, no. May, p. 115402, 2020.

[34] A. García, J. Monsalve-serrano, R. L. Sari, and S. Martinez-boggio, “An optical investigation of thermal runway phenomenon under thermal abuse conditions,” *Energy Convers. Manag.*, vol. 246, p. 114663, 2021.

[35] R. S. G. Baert, P. J. M. Frijters, B. Somers, C. C. M. Luijten, and W. De Boer, “Design and operation of a high pressure, high temperature cell for HD diesel spray diagnostics: Guidelines and results,” *SAE Tech. Pap.*, 2009.

[36] J. V. Pastor, A. García, C. Micó, and A. A. García-Carrero, “Experimental study of influence of Liquefied Petroleum Gas addition in Hydrotreated Vegetable Oil fuel on ignition delay, flame lift off length and soot emission under diesel-like conditions,” *Fuel*, vol. 260, no. July 2019, p. 116377, 2020.

[37] J. V. Pastor, A. García, C. Micó, and F. Lewiski, “Simultaneous high-speed spectroscopy and 2-color pyrometry analysis in an optical compression ignition engine fueled with OMEX-diesel blends,” *Combust. Flame*, vol. 230, no. x, 2021.